Bulletin of Natural Sciences Research
Vol.15, No. 1, 2025, pp. 27-33.
DOI: https://doi.org/10.5937/bnsr15-61823
Original Scientific Paper

STRUCTURAL AND ELECTROCHEMICAL PROPERTIES OF SYNTHESIZED NANOSTRUCTURED $Ca_{0.9}Er_{0.1}MnO_3$ BY HYDRAZINE NITRITE PROCEDURE

TIJANA B. VLAŠKOVIĆ[1], MILENA ROSIĆ[2], BRANKA B. PETKOVIĆ[1], BOJANA B. LABAN[1*]

[1]Faculty of Sciences and Mathematics, University of Priština in Kosovska Mitrovica, Kosovska Mitrovica, Serbia
[2]Institute of Nuclear Sciences "Vinča", National Institute of the Republic of Serbia, University of Belgrade, Serbia

ABSTRACT

Synthesis, structural, and electrochemical properties of nanostructured powders $Ca_{0.9}Er_{0.1}MnO_3$ with perovskite-type crystal were studied. Nanopowders were prepared by the combustion method using the hydrazine nitrite procedure (HNP), which involves mixing metal nitrate salts (Ca, Mn, Er) in a stoichiometric ratio and varying the quantity of added hydrazine. In this synthetic procedure, the aim is to adjust the amount of hydrazine in order to control the combustion of the reactions, obtain the required amount of fuel energy, but also the amount that will complex the reactants in the mixture. The powders obtained by hydrazine nitrate synthesis were then calcined for 15 minutes at temperatures of 800, 900, and 1000 °C. Characterization of the synthesized and calcined samples was performed using advanced techniques such as X-ray diffraction (XRD), Fourier-transform infrared spectroscopy (FTIR), and electrochemical measurements. The results clearly indicate that the amount of hydrazine added is crucial in preparing the $Ca_{0.9}Er_{0.1}MnO_3$ sample. This highlights the importance of precise hydrazine dosage in optimizing the synthesis process to enhance the material's properties. Further, the electrochemical properties of the obtained perovskite nanopowders were investigated by cyclic voltammetry (CV) and electrochemical spectroscopic impedance (EIS) on perovskite-modified carbon paste electrodes. Electrochemical measurements showed improved electrochemical properties of perovskite-modified carbon paste electrodes compared to bare carbon paste electrode (CPE). The electrode modified with the material synthesized with the smallest amount of hydrazine presented the best results.

Keywords: Perovskites, Hydrazine nitrite procedure, Electrochemical.

INTRODUCTION

Perovskite-type compounds are special materials that share a similar crystal structure and have garnered significant attention in both scientific research and practical applications due to their diverse and unique properties, including ferroelectricity, ferromagnetism, fast-ion conductivity, superconductivity, etc. The term "perovskite-type structure" originates from the mineral calcium titanate ($CaTiO_3$), the first material identified with this specific crystalline structure. It was discovered by geologist Gustav Rose in the Ural Mountains in 1839 and named "perovskite" in honor of the Russian mineralogist Count Lev Alekseevich von Perovsky (Katz, 2020). This name refers to any compound of the formula ABX_3, with a similar ionic crystalline structure. Among various compounds with a perovskite structure, perovskite oxide materials with the general formula ABO_3 attracted the attention of researchers due to their specific chemical and physical properties (Bispo-Jr et al., 2022). The ABO_3 perovskite structure consists of a framework formed by corner-sharing octahedra. Distortions of the octahedra often occur in these structures due to deviations from ideal values of the ion size ratios between the A, B, and O sites of the crystal. Additionally, the A or B cations may exhibit characteristic sizes and valences that can result in oxygen non-stoichiometry, including excess and/or deficiency of oxygen (Kuganathan & Chroneos, 2021).

There are various synthetic methods for the formation of perovskite-type nanomaterials, which can be categorized by three main approaches: solid-state, liquid-state, and gas-state synthesis (Bayode et al., 2024). In this manner, methods such as the mechanical ball-milling method, combustion method, co-precipitation method, and sol-gel chemical method have been employed (Ansari et al., 2020; Bayode et al., 2024; Yadav et al., 2020; Tadić et al., 2016). The challenge is to control the size, crystallinity, morphology, shape, and properties, and to form nanomaterials for specific purposes and from different elements. The choice of methods for perovskite synthesis affects the physical and chemical properties of the material. Additionally, perovskite oxides, due to their multiple oxidation states at the B-site, possess redox properties, and they have been found to have potential applications as electrode materials for electrochemical sensors (Shimizu et al., 1996; Durai & Badhulika, 2022).

* Corresponding author:tijanavlaskovicpantovic@gmail.com

Transition metal-containing perovskite oxides exhibit excellent structural flexibility, enabling the placement of various doping cations on either the A or B site while maintaining the perovskite-type framework (Yang et al., 2017; Kuganathan & Chroneos, 2021). Among these materials, $CaMnO_3$ is studied because it has been found to have applications in electrocatalysis, Li-ion batteries, and electronics, among others (Kuganathan & Chroneos, 2021). Doped perovskite manganites have a general formula $A_{1-x}Re_xMnO_3$, where A is an alkali earth element, and Re is a rare-earth element (Rosić et al., 2015; Rosić et al., 2011). In this perovskite-type oxide, manganese can exist in two oxidation states, Mn^{3+} and Mn^{4+}, to maintain charge neutrality. It was found that rare-earth element (Re) atoms occupy the A sites, while smaller cations occupy the B sites (Dukić et al., 2009). Previous work reports that Gd occupies the A sites, because Gd^{3+} is a cation that is significantly larger than the Mn cation, and substitution of Ca with Gd will affect the valence of Mn (Rosić et al., 2011). In undoped $CaMnO_3$, Mn^{4+} ions exhibit antiferromagnetic ordering. However, Gd^{3+} doping introduces Mn^{3+} ions, whose ferromagnetic double exchange interaction with Mn^{4+} leads to the formation of ferromagnetic clusters within an antiferromagnetic matrix (Rosić et al., 2011; Rosić et al., 2015). Additionally, previous research has reported that the substitution of cations in perovskite-type oxides can alter the crystal symmetry from orthorhombic (*Pnma*) to tetragonal (*I4/mcm*) (Srivastava et al., 2015). The incorporation of rare-earth elements into perovskite oxides is primarily governed by ionic size compatibility between host and dopant cations. In $CaMnO_3$, calcium occupies the A-site of the perovskite lattice, with an effective ionic radius of approximately 1.12 Å for Ca^{2+} in 12-fold coordination (Shannon, 1976). Erbium, by comparison, has a smaller ionic radius of about 1.004 Å for Er^{3+} in 8-fold coordination (Shannon, 1976). Despite this size difference, the mismatch remains within the tolerance limits of the perovskite structure, enabling partial substitution of Ca^{2+} by Er^{3+}. Such substitution is expected to induce local lattice distortions, modify the electronic environment, and allow for tuning of functional properties including electrical transport, magnetic ordering, optical response, and defect behavior (Kuganathan & Chroneos, 2021; Xia et al., 2025). The primary objective of this work is to investigate the structural and electrochemical properties of Er^{3+}-doped $CaMnO_3$ oxides, aiming to clarify the role of Er substitution and explore its potential for applications in advanced functional materials, such as thermoelectrics, solid oxide fuel cells, and optoelectronic devices.

In this work, the possibility of forming a nanostructured solid solution with a nominal composition of $Ca_{0.9}Er_{0.1}MnO_3$ was studied using a modified hydrazine nitrite procedure (HNP). Structural and electrochemical properties were investigated.

EXPERIMENTAL

Chemicals

All used chemicals were of analytical grade. Calcium-nitrate tetrahydrate ($Ca(NO_3)_2 \cdot 4H_2O$), Manganese-nitrate hydrate ($Mn(NO_3)_2 \cdot H_2O$), Erbium-nitrate pentahydrate ($Er(NO_3)_3 \cdot 5H_2O$), Hydrazine hydrate ($N_2H_2 \cdot H_2O$), Glassy carbon powder, Liquid paraffin (C_nH_{2n+2}), and Potassium with complex ion $[Fe(CN)_6]^{3-/4-}$, all >99.9% purity (Merck). All solutions were prepared using water purified with a Millipore Milli-Q system.

Synthesis of nanostructured powders

To achieve enhanced control over the stoichiometry, structure, and phase purity of metal oxides, the avoidance of the brute force method remains a fundamental approach in the synthesis of new materials. Starting chemicals used for the HNP (hydrazine nitrate procedure) synthesis of powders were nitrate salts of Ca, Mn, and Er. Hydrazine played a double role as both a complexant and a fuel. The composition of the reacting mixtures was calculated based on the nominal composition of the final reaction product. The principles of propellant chemistry (Patil, 2008) were applied to calculate the composition of the reacting mixtures. In stoichiometric redox reactions between a fuel and an oxidizer, it is essential to define the ratio of the net oxidizing valences of the metal nitrate to the net reducing valences of the fuel. It is essential to gain this understanding to enhance our knowledge and applications in this specific field. By convention, the valencies of nitrogen, oxygen, hydrogen, calcium, erbium, and manganese are set as 0, 2–, 1+, 2+, 3+, and 4+, respectively. Using the valencies of these individual elements, the reducing valence of hydrazine, $N_2H_4H_2O = 2(0)+4(+1)+2(+1)+(-2) = 4$; it works out to be 4+, while $Ca(NO_3)_3$, $Er(NO_3)_3$, and $Mn(NO_3)_3$ work out to be 15–, respectively. We add these values based on Equations (1) and divide them by 4 (the value for hydrazine). For producing one mole of $Ca_{0.9}Er_{0.1}MnO_3$, through the stoichiometric reactions (1), there will be −20.5/4 = 5.125 moles of hydrazine, which is required. According to the chemical equations, $Ca_{0.9}Er_{0.1}MnO_3$ powder was prepared:

$$N_2H_4 \cdot H_2O + 0.9\,Ca(NO_3)_2 \cdot 4\,H_2O + Mn(NO_3)_2 \cdot H_2O + 0.1\,Er(NO_3)_3 \cdot 5\,H_2O + 6.1\,O_2 \rightarrow Ca_{0.9}Er_{0.1}MnO_3 + 6.1\,NO_2 + 8.1\,H_2O. \quad (1)$$

The starting mixture of the selected composition $Ca_{0.9}Er_{0.1}MnO_3$ was synthesized using a stoichiometric ratio of metal salts and varying amounts of hydrazine compared to the molar ratio from Equation 1. In the HNP method, metal nitrate salts and hydrazine were mixed in a molar ratio: 1 molMn : 1 molCa+Er : 1/6 (0.17 mol) N_2H_4; 1 molMn : 1 molCa+Er : 1/3 (0.33 mol) N_2H_4; and 1 molMn : 1 molCa+Er : 1/2 (0.5 mol) N_2H_4.

In a 1-liter beaker, the calculated masses of the appropriate chemicals were combined and dissolved in a small amount of water, after which three drops of concentrated nitric acid were added. The mixture was heated in the temperature range of 60 – 70 °C. After the reaction was completed, a bulky material was obtained. The second step of the experiment is calcination in an annealing furnace at three different temperatures, 800, 900, and 1000°C. For each sample, we annealed the material for 15 minutes at a given temperature. When applying this method, the most important factor is the molar ratio of hydrazine and nitrate ions in the mixture, as the reaction temperature (due to exothermicity) is higher, resulting in a larger crystal size of the resulting material, i.e., the initial reactants will react more effectively.

RESULTS AND DISCUSSION

XRD Analysis

The XRD patterns of the $Ca_{0.9}Er_{0.1}MnO_3$ powder samples were obtained after combustion reaction (HNP), calcination at 800, 900, and 1000 °C, and different molar ratios are shown in Figure 1a–c.

Following the combustion reaction, the XRD patterns of the resulting powders appeared to be amorphous. This could likely be attributed to inadequate heat generated during the auto-ignition process (Rosić et al., 2011).

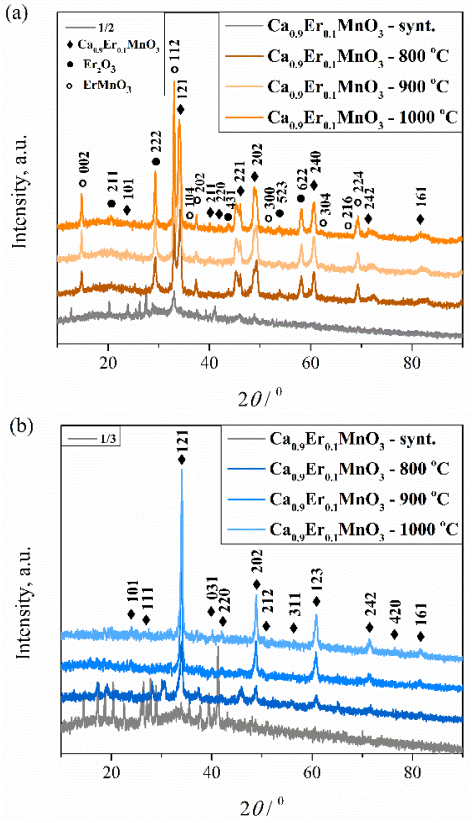

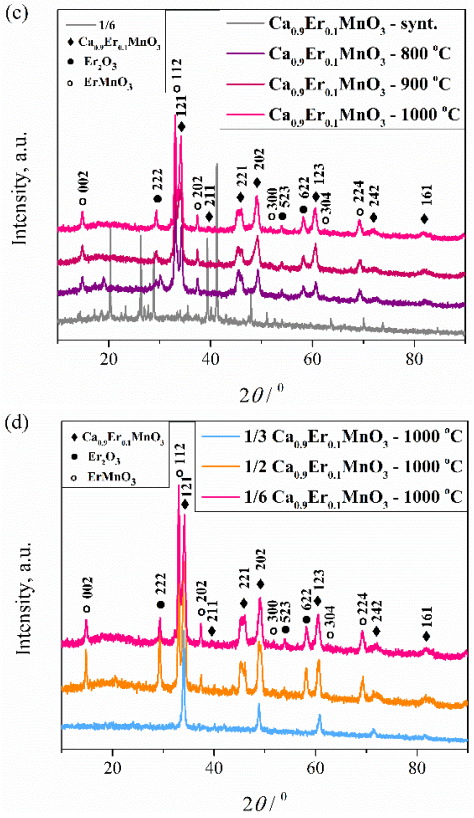

Figure 1. XRD patterns of $Ca_{0.9}Er_{0.1}MnO_3$ powders after combustion, different calcination temperatures, and molar ratios: (a) 1/2-$Ca_{0.9}Er_{0.1}MnO_3$, (b) 1/3-$Ca_{0.9}Er_{0.1}MnO_3$, (c) 1/6-$Ca_{0.9}Er_{0.1}MnO_3$, (d) Comparison of powder samples at the same 1000 °C, but different molar ratios for different amounts of hydrazine: 1/2 – 0.17 molHy, 1/3 – 0.33 molHy, and 1/6 – 0.5 molHy.

XRD patterns of the $Ca_{0,9}Er_{0,1}MnO_3$ powders after calcinations at 800, 900, and 1000 °C with 0.17 and 0.5 mol hydrazine in the initial mixture (Figure 1a and 1c), show the separation of three phases: $CaMnO_3$ (ICSD #153238, *Pnma* N° 62), $ErMnO_3$ (ICSD #162201, *P 63 c m* N°185), and ErO_3 (ICSD #33656, *I 21 3* N°199)(International Crystallographical Database (ICDD)). The formation of these three phases suggests that the violent combustion reaction occurred too rapidly for hydrazine, which serves as both a fuel and a complexant, to effectively perform its dual role. As a result, it did not have sufficient time to bind all the elements present into the perovskite phase. In contrast to the two previously mentioned samples, a monophasic sample was formed in the sample with 0.33 moles of hydrazine in the mixture; an appropriate proportion of fuel was obviously added. Based on the diffractogram (Figure 1b), the calcination temperature for $Ca_{0.9}Er_{0.1}MnO_3$ is in the range of 900 to 1000 °C. A change in the unit cell parameters was observed, but it was not significant due to the small difference in ionic radii between Ca^{2+} and Er^{3+}. The most noticeable changes occurred in the

volume and parameter b, while parameters a and c showed negligible differences (see Table 1).

Table 1. Percentage and cell parameters [Å, degree] and volume [Å^3] of the unit cell for $Ca_{0.9}Er_{0.1}MnO_3$ phases were observed directly in samples with 0.33 moles of hydrazine in the mixture that have beencalcinated at 900 and 1000 °C, respectively. The data were obtained using the software package Powder Cell (Kraus & Nolze, 1996, http://powdercell-for-windows.software.informer.com/2.4/) and compared with data from the reference (International Crystallographical Database (ICDD)) marked with *.

$CaMnO_3$* ICSD #153238	$Ca_{0.9}Er_{0.1}MnO_3$ 900 °C	$Ca_{0.9}Er_{0.1}MnO_3$ 1000 °C
a=5.2812 b=7.457 c=5.2753 V=207.75	a=5.2766 b=7.5110 c=5.2741 V=209.03	a=5.2723 b=7.4898 c=5.2747 V=208.29
	Rp=5.62 Rwp=7.40 Rexp=0.39	Rp=6.08 Rwp=8.21 Rexp=0.51
	Size 33.32 Strain 0.0029	Size 35.63 Strain 0.0026

While not all peaks are broad, they tend toward that shape and exhibit a moderate intensity, suggesting a nanocrystalline nature, confirmed by a crystallite size of approximately 35 nm. Figure 1d shows a clear difference when visually comparing observed samples.

FTIR spectroscopy

The FTIR spectra of as-prepared and calcinated $Ca_{0.9}Er_{0.1}MnO_3$nanopowders are presented in Figure 2. In Figure 2a, FTIR spectra for as-prepared $Ca_{0.9}Er_{0.1}MnO_3$ are presented using different amounts of hydrazine: 0.17 mol, 0.33 mol, and 0.5 mol.

The FTIR spectra of as-prepared materials (Fig. 2a) show that the band from hydrazine prevails. In contrast, band characteristics of M – O bonds in perovskite (400 – 700 cm^{-1}) are slightly visible, indicating that the reaction is not completed and that there is unreacted hydrazine present in samples. The FTIR spectrum bands come from the vibrational mode of hydrazine: N – H stretching, NH bending, and N – N stretching, and the torsional oscillation (Giguère & Liu, 1952). Pairs of bands at 814 and 855 cm^{-1} are from the symmetric ν_6 NH_2 wagging mode, along with the band at 742 cm^{-1} which is due to ν_7 wagging mode (Giguère and Liu, 1952). Bands that come from N – H stretching vibrations are positioned at 3475 and 3555 cm^{-1}, bands positioned at 1635 and 1800 cm^{-1} are from N – H bending vibrations (Giguère & Liu, 1952), while bands at 1040, 1319, 1450 cm^{-1} are from nitrates (Mihaylov et al., 2021). The fundamental N – N vibration is an essentially nonpolar bond, it is expected to be weak in the infrared spectrum, and it falls in a region of the NH wagging modes (Giguère & Liu, 1952).

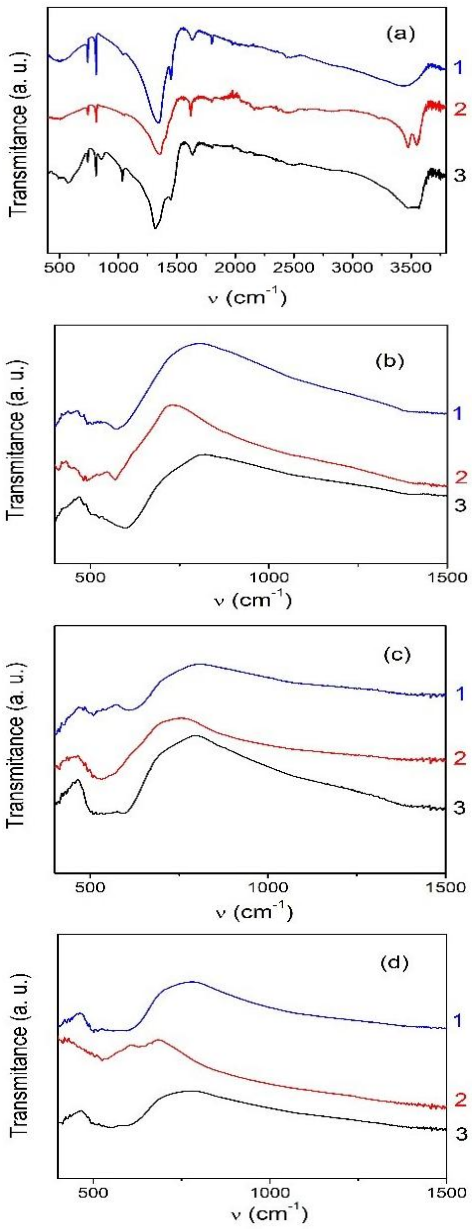

Figure 2. FTIR spectra of $Ca_{0.9}Er_{0.1}MnO_3$nanopowders: a) as-prepared, b) calcinated at 800 °C, c) calcinated at 900 °C, and d) calcinated at 1000 °C, for different amounts of hydrazine: 1 – 0.17 mol Hy, 2 – 0.33 mol Hy, and 3 – 0.5 mol Hy.

After calcination of synthesized materials, at 800, 900, and 1000 °C (Fig. 2 b, c, and d), vibrational modes that come from M – O bonds are more visible, while the band that comes from hydrazine disappears. For M – O bonds (M = Ca, Er, Mn), vibration bands are expected to be in a lower region of wavenumber, 400 – 600 cm^{-1}. From Figure 2 (b, c, and d),

observing the spectra in the wavenumber region of 400 – 600 cm^{-1}, it can be seen that changes are presented due to hydrazine concentration and temperature calcination, indicating a structural change in the materials. FTIR results are in good agreement with XRD results. For a more detailed analysis of the FTIR spectra, we selected the spectra of $Ca_{0.9}Er_{0.1}MnO_3$ synthesized with 0.33 mol of hydrazine and calcined at 900 °C.

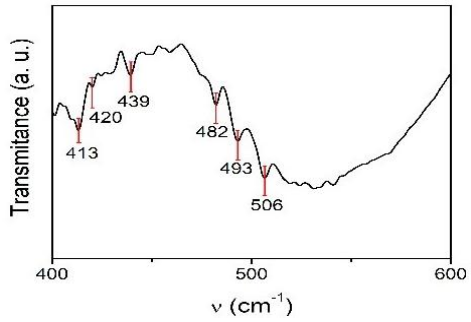

Figure 3. FTIR spectra for $Ca_{0.9}Er_{0.1}MnO_3$ synthesized with 0.33 mol of hydrazine and calcinated at 900 °C.

Figure 3presents the FTIR spectra of the synthesized perovskite material $Ca_{0.9}Er_{0.1}MnO_3$, calcined at 900 °C, within the 400–1000 cm^{-1} range, highlighting the positions of characteristic infrared bands. The observed bands are located at 413, 420, 439, 482, 493, and 506 cm^{-1}, along with a broad band spanning 520–570 cm^{-1}. All identified infrared bands are situated below 700 cm^{-1}, corresponding to vibrations within the Ca–Er–Mn–O framework. These results are consistent with previous FTIR studies of perovskite oxides (Macan et al., 2020, Mary et al., 2024, Rosić et al., 2015, Ansari et al., 2020). It can be observed that no bands appear above 700 cm^{-1} in the FTIR spectra (Fig. 2b, c, and d), indicating the elimination of NO_3^- groups from nitrates and the disappearance of hydrazine-related bands after calcination. The observed bands (Fig. 3) are assigned to O–Mn–O/Mn–O–Mn bending vibrations, and Mn–O asymmetric stretching vibrations of MnO_6octahedra (Macan et al., 2020, Mary et al., 2024). Compared to the position of infrared bands of $CaMnO_3$ (Macan et al., 2020), they are slightly moved due to Er doping, indicating the influence of Er on the crystal lattice.

However, the interpretation of spectra is complicated by the possibility that spectral differences may also arise from variations in the degree of edge-sharing between MnO_6 ctahedra (Julien & Massot, 2003). The full assignment of the bands in the 600–400 cm^{-1} range, therefore, requires further work.

Electrochemical properties of $Ca_{0.9}Er_{0.1}MnO_3$

$Ca_{0.9}Er_{0.1}MnO_3$ samples with different amounts of hydrazine (1 – 0.17 mol Hy, 2 – 0.33 mol Hy, and 3 – 0.5 mol Hy) were employed as electrode modifier and CV and EIS measurements were done in the presence of a stationary 5 mM $K_3[Fe(CN)]_6/K_4[Fe(CN)]_6$ (1:1) mixture as a redox probe in 0.1 M KCl solution. Based on cyclic voltammograms in Figure 4a, all modified electrodes showed improved electrocatalytic behavior compared to bare CPE. It is obvious that the material synthesized with the smallest amount of Hy was the material with the highest current conductivity. Anodic peak related to the oxidation of $Fe^{2+} \rightarrow Fe^{3+}$ was observed at 0.303 V, while the cathodic peak for the opposite reaction was observed at 0.157 V, with peak potential separation, ΔE, of 0.146 V. This suggested that the Fe^{2+}/Fe^{3+} redox couple on the modified carbon paste electrode showed a quasi-reversible behavior.

The CV results were further compared to EIS measurements presented at the graph Fig 4b: the smallest semicircle, formed by points at lower frequencies indicated better conductivity, the promoted electron exchange transfer on the electrode surface and improved catalytic activity.

CVs on different scan rates (10, 25, 50, 75, 100, 125, and 150 mV/s) for the modified electrode with the smallest amount of Hy (1 at CPE) are given in Figure 4c. A derivative linear plot obtained from it, which presents current vs. the square root of scan rate (Fig. 4d), shows that the dominant process at the electrode surface is the diffusion of electroactive species (Fe^{3+}/Fe^{2+}), while absorption and other processes are negligible.The linearity is described by Equation 2 obtained by regression analysis of the results, with an excellent correlation coefficient of 0.997.

$$I(\mathrm{A}) = -5.78\times10^{-6} + 1.31\times10^{-5}\times v^{1/2}\,(\mathrm{mV/s})^{1/2};\quad (\mathrm{R} = 0.997). \tag{2}$$

From Figure 4d, and in the same way, recorded and analyzed results obtained from the CV profiles of the other modified electrodes (2 at CPE, 3 at CPE and bare CPE), the active electrode surface has been calculated, using Randles–Sevcik formula (3) for a reversible (and quasi-reversible) process (Rezaei and Damiri, 2008):

$$\mathrm{Ip} = 0.4463\times\left(\mathrm{F}^3/\mathrm{RT}\right)^{1/2}\times \mathrm{n}^{3/2}\times \mathrm{A}_0\times \mathrm{D}_0{}^{1/2}\times \mathrm{C}^{1/2}. \tag{3}$$

where T is 298 K, R is 8.314 J $Kmol^{-1}$, F is 96 480 C mol^{-1}, n is 1, D_0 is 7.6 × 10^{-6} cm^2 s^{-1} and C is 5 mM of $K_3[Fe(CN)]_6/K_4[Fe(CN)]_6$.The active areas of bare CPE and 1, 2 and 3 samples in CPE were $4.88\times10^{-2}cm^2$, 1.02×10^{-2} cm^2, 7.30×10^{-2} cm^2 and 5.50×10^{-2} cm^2, respectively.

Bearing in mind the results obtained by applied electrochemical measurements and calculations, the perovskite nanopowder prepared with the smallest amount of Hy showed up as potentially the most suitable for application in electroanalysis and catalysis, although excellent results and shape of the CV profile are also obtained by a material with slightly more Hy in it (2 at CPE).

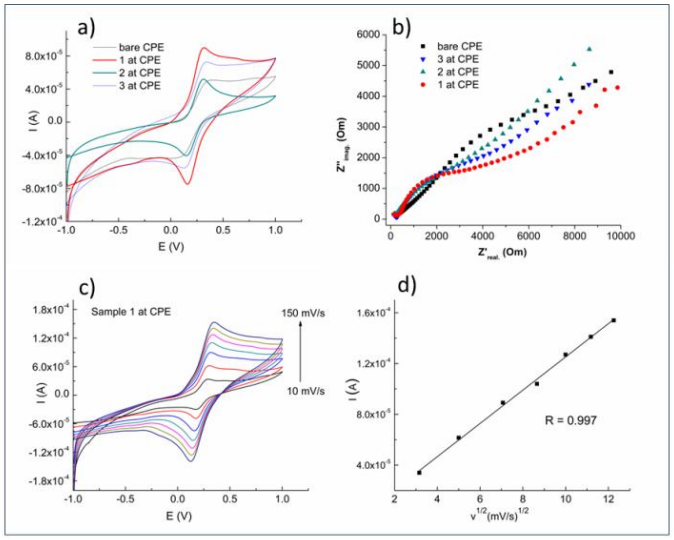

Figure 4. a) CV profiles of bare and perovskite-modified electrodes in in 0.1M KCl test solution containing 5 mM $[Fe(CN)_6]^{3-/4-}$ redox couple (scan rate 50 mV/s); b) EIS measurements in the same test solution; c) CV profiles at modified 1 at CPE in different scan rates (10, 25, 50, 75, 100, 125 and 150 mV/s); d) Graph of I *vs*square root of scan rate obtained from CV profiles on previous figure.

XRD analysis revealed that the sample synthesized with the lowest hydrazine concentration consisted of three phases: $CaMnO_3$, $ErMnO_3$, and Er_2O_3. The enhanced electrical conductivity observed for this material is in line with previous findings that multiphase perovskite systems often surpass their single-phase analogs in electrochemical performance. This improvement can be explained by several factors: the presence of multiple phases creates structural defects and interfacial regions that act as fast diffusion pathways for oxygen ions and charge carriers; secondary oxides contribute additional catalytic functionality; and local modifications of the chemical environment, such as variations in oxygen vacancy concentration and Mn oxidation states, further promote ionic/electronic conductivity and provide active sites for electrochemical reactions (Du et al., 2014). Previous investigations of multiphase $CaMnO_3/CaMn_2O_4$ systems have shown that the presence of phase boundaries and controlled microstructural features plays a critical role in enhancing both bulk and surface transport. Such improvements are directly relevant to electrochemical applications, where they translate into higher electronic conductivity and superior functional performance (Kanas et al., 2022).

CONCLUSION

Nanopowders with the nominal composition $Ca_{0.9}Er_{0.1}MnO_3$ were successfully synthesized by the combustion method using the hydrazine nitrate procedure (HNP). The influence of the hydrazine content on phase formation was systematically investigated. XRD analysis revealed the presence of three crystalline phases, and it was determined that a hydrazine ratio of 0.33 mol provides the most favorable conditions for obtaining a near-monocrystalline structure. FTIR spectra confirmed the incorporation of Er into the perovskite lattice. Thermal treatment studies showed that higher calcination temperatures improved crystallinity and promoted grain growth. Electrochemical measurements demonstrated that the highest electrical conductivity was achieved in the sample prepared with the lowest hydrazine content, which can be attributed to the formation of multiphase perovskite systems.

ACKNOWLEDGMENTS

This research was funded by the Ministry of Science, Technological Development and Innovation of the Republic of Serbia, based on Contract no. 451-03-137/2025-03/200123, Faculty of Sciences and Mathematics University of Priština in Kosovska Mitrovica, Project Number IJ-2301 and 451-03-136/2025-03/200017 through the realization of research theme 1702514 by "Vinča" Institute of Nuclear Sciences—National Institute of the Republic of Serbia, University of Belgrade.

REFERENCES

Ansari, A. A., Adil, S. F., Alam, M., Ahmad, N., Assal, M. E., Labis, J. P. & Alwarthan, A. 2020. Catalytic performance of the Ce-doped $LaCoO_3$ perovskite nanoparticles. Scientific Reports, 10, 15012. https://doi.org/10.1038/s41598-020-71869-z

Bayode, A. A., Ore, O. T., Nnamani, E. A., Sotunde, B., Koko, D. T., Unuabonah, E. I., Helmreich, B. & Omorogie, M. O. 2024. Perovskite Oxides: Syntheses and Perspectives on Their Application for Nitrate Reduction. ACS Omega, 9, pp. 19770-19785. https://pubs.acs.org/doi/10.1021/acsomega.4c01487

Bispo-Jr, A. G., de Morais, A. J., Calado, C. M. S., Mazali, I. O. & Sigoli, F. A. 2022. Lanthanide-doped luminescent perovskites: A review of synthesis, properties, and applications. Journal of Luminescence, 252, 119406. https://doi.org/10.1016/j.jlumin.2022.119406

Du, J., Zhang, T., Cheng, F., Chu, W., Wu, Z. & Chen, J. 2014. Nonstoichiometric Perovskite $CaMnO_3-\delta$ for Oxygen Electrocatalysis with High Activity. Inorganic Chemistry, 53, 9106-9114. https://pubs.acs.org/doi/10.1021/ic501631h

Dukić, J., Bošković, S. & Matović, B. 2009. Crystal structure of Ce-doped $CaMnO_3$ perovskite. Ceramics International, 35, pp. 787-790. https://doi.org/10.1016/j.ceramint.2008.02.023

Durai, L. & Badhulika, S. 2022. Current Challenges and Developments in Perovskite-Based Electrochemical Biosensors for Effective Theragnostics of Neurological Disorders. ACS Omega, 7, pp. 39491-39497. https://pubs.acs.org/doi/10.1021/acsomega.2c05591

Giguère, P. A. & Liu, I. D. 1952. On the Infrared Spectrum of Hydrazine. The Journal of Chemical Physics, 20, pp. 136-140. https://doi.org/10.1063/1.1700155

Julien, C. M. & Massot, M. 2003. Lattice vibrations of materials for lithium rechargeable batteries I. Lithium manganese oxide spinel. Materials Science and Engineering: B, 97, pp. 217-230. https://doi.org/10.1016/S0921-5107(02)00582-2

Kanas, N., Williamson, B. A. D., Steinbach, F., Hinterding, R., Einarsrud, M.-A., Selbach, S. M., Feldhoff, A. & Wiik, K. 2022. Tuning the Thermoelectric Performance of $CaMnO_3$-Based Ceramics by Controlled Exsolution and Microstructuring. ACS Applied Energy Materials, 5, pp. 12396-12407. https://pubs.acs.org/doi/10.1021/acsaem.2c02012

Katz, E. A. 2020. Perovskite: Name Puzzle and German-Russian Odyssey of Discovery. Helvetica Chimica Acta, 103, e2000061. https://doi.org/10.1002/hlca.202000061

Kraus, W. & Nolze, G. 1996. POWDER CELL - a program for the representation and manipulation of crystal structures and calculation of the resulting X-ray powder patterns. Journal of Applied Crystallography, 29, pp. 301-303. https://doi.org/10.1107/S0021889895014920

Kuganathan, N. & Chroneos, A. 2021. Defect and dopant properties in $CaMnO_3$. AIP Advances, 11, 055106. https://doi.org/10.1063/5.0048401

Macan, J., Brleković, F., Kralj, S., Supina, A., Gracin, D., Šantić, A. & Gajović, A. 2020. Soft chemistry synthesis of $CaMnO_3$ powders and films. Ceramics International, 46, pp. 18200-18207. https://doi.org/10.1016/j.ceramint.2020.04.142

Mary, S. B., Mohan, K. S. & Krishnan, M. M. 2024. Effect of A-site and B-site ion substitution on the electrical and thermoelectric properties of nanostructured perovskite $CaMnO_3$. Journal of Materials Science: Materials in Electronics, 35, 600. https://doi.org/10.1007/s10854-024-12351-8

Mihaylov, M. Y., Zdravkova, V. R., Ivanova, E. Z., Aleksandrov, H. A., Petkov, P. S., Vayssilov, G. N. & Hadjiivanov, K. I. 2021. Infrared spectra of surface nitrates: Revision of the current opinions based on the case study of ceria. Journal of Catalysis, 394, pp. 245-258. https://doi.org/10.1016/j.jcat.2020.06.015

Patil, K. C. H., M. S.; Rattan, T.; Aruna, S. T. 2008. Solution Combustion Synthesis of Oxide Materials. Chemistry of Nanocrystalline Oxide Materials. Singapore: World Scientific Publishing Co. Pte. Ltd. https://doi.org/10.1142/6754

Rezaei, B. & Damiri, S. 2008. Voltammetric behavior of multi-walled carbon nanotubes modified electrode-hexacyanoferrate(II) electrocatalyst system as a sensor for determination of captopril. Sensors and Actuators B: Chemical, 134, pp. 324-331. https://doi.org/10.1016/j.snb.2008.05.004

Rigaku 2011. PDXL Integrated X-Ray Powder Diffraction Software. In: RIGAKU (ed.). Tokyo, Japan.

Rosić, M., Kljaljević, L., Jordanov, D., Stoiljković, M., Kusigerski, V., Spasojević, V. & Matović, B. 2015. Effects of sintering on the structural, microstructural and magnetic properties of nanoparticle manganite $Ca_{1-x}Gd_xMnO_3$ (x=0.05, 0.1, 0.15, 0.2). Ceramics International, 41, pp. 14964-14972. https://doi.org/10.1016/j.ceramint.2015.08.041

Rosić, M., Logar, M., Devečerski, A., Prekajski, M., Radosavljević-Mihajlović, A., Kusigerski, V., Spasojević, V. & Matović, B. 2011. Synthesis, structural and magnetic properties of nanostructured $Ca_{0.9}Gd_{0.1}MnO_3$ obtained by modified glycine nitrate procedure (MGNP). Ceramics International, 37, pp. 1313-1319. https://doi.org/10.1016/j.ceramint.2010.12.015

Shannon, R. D. 1976. Revised effective ionic radii and systematic studies of interatomic distances in halides and chalcogenides. Acta Crystallographica Section A, 32, pp. 751-767. https://doi.org/10.1107/S0567739476001551

Shimizu, Y., Komatsu, H., Michishita, S., Miura, N. & Yamazo, N. 1996. Sensing characteristics of hydrogen peroxide sensor using carbon-based electrode loaded with perovskite-type oxide. Sensors and Actuators B: Chemical, 34, pp. 493-498. https://doi.org/10.1016/S0925-4005(97)80021-4

Srivastava, D., Azough, F., Freer, R., Combe, E., Funahashi, R., Kepaptsoglou, D. M., Ramasse, Q. M., Molinari, M., Yeandel, S. R., Baran, J. D. & Parker, S. C. 2015. Crystal structure and thermoelectric properties of Sr–Mo substituted $CaMnO_3$: a combined experimental and computational study. Journal of Materials Chemistry C, 3, pp. 12245-12259. https://doi.org/10.1039/C5TC02318A

Tadić, M., Marković, D., Panjan, M. & Spasojević, V. 2016. Solution combustion synthesis method and magnetic properties of synthesized polycrystalline calcium manganite $CaMnO_{3-\delta}$ powder. Ceramics International, 42, pp. 19365-19371. https://doi.org/10.1016/j.ceramint.2016.09.109

Xia, Z.-R., Li, R.-Q., Liu, F.-F., Tong, Y., Zheng, Q.-H., Ping, Z.-Y., Zhao, W., Zhou, W.-W. & Song, M.-J. 2025. Upconversion and Downconversion Luminescence of $CaLaLiTeO_6$:Mn^{4+}/Er^{3+} Phosphors for Dual-Mode Optical Thermometry and Anti-Counterfeiting Application. Inorganics, 13, 308. https://doi.org/10.3390/inorganics13090308

Yadav, R. S., Kumar, D., Kanwal, M., Singh, A. K. & Rai, S. B. 2020. Synthesis Techniques and Applications of Perovskite Materials. In: TIAN, H. (ed.) Perovskite Materials, Devices and Integration. Rijeka: Intech Open. DOI: 10.5772/intechopen.86794

Yang, P., Tai, B., Wu, W., Zhang, J.-M., Wang, F., Guan, S., Guo, W., Lu, Y. & Yang, S. A. 2017. Tailoring lanthanide doping in perovskite $CaTiO_3$ for luminescence applications. Physical Chemistry Chemical Physics, 19, pp. 16189-16197. https://doi.org/10.1039/C7CP01953J

International Crystallographical Database (ICDD); PDF-2, Release 2023; ICDD: Newtown Square, PA, USA, 2012.

https://icsd.products.fiz-karlsruhe.de/ (accessed on 10 September 2025).

http://powdercell-for-windows.software.informer.com/2.4/ (accessed on 10 September 2025).